



We are Nitinol.™

## **Fatigue and Durability of Nitinol Stents**

A.R. Pelton, V. Schroeder, M.R. Mitchell, Xiao-Yan Gong, M. Barney, and S.W. Robertson,

J Mech Behavior Biomed Mater, 1, 153–164 (2008).

2008

Provided for non-commercial research and education use.  
Not for reproduction, distribution or commercial use.



This article was published in an Elsevier journal. The attached copy is furnished to the author for non-commercial research and education use, including for instruction at the author's institution, sharing with colleagues and providing to institution administration.

Other uses, including reproduction and distribution, or selling or licensing copies, or posting to personal, institutional or third party websites are prohibited.

In most cases authors are permitted to post their version of the article (e.g. in Word or Tex form) to their personal website or institutional repository. Authors requiring further information regarding Elsevier's archiving and manuscript policies are encouraged to visit:

<http://www.elsevier.com/copyright>



ELSEVIER

available at [www.sciencedirect.com](http://www.sciencedirect.com)journal homepage: [www.elsevier.com/locate/jmbbm](http://www.elsevier.com/locate/jmbbm)

## Research paper

## Fatigue and durability of Nitinol stents

A.R. Pelton<sup>a,\*</sup>, V. Schroeder<sup>a</sup>, M.R. Mitchell<sup>b</sup>, Xiao-Yan Gong<sup>c</sup>, M. Barney<sup>a</sup>, S.W. Robertson<sup>d</sup><sup>a</sup> Nitinol Devices and Components, 47533 Westinghouse Dr., Fremont, CA 94539, United States<sup>b</sup> Mechanics and Materials Consulting, LLC, 4447 Acrete Ln., Flagstaff, AZ 86004, United States<sup>c</sup> Medical Implant Mechanics, LLC, 26895 Aliso Creek Road, Suite #B716, Aliso Viejo, CA 92656, United States<sup>d</sup> Cordis Corporation, 47533 Westinghouse Dr., Fremont, CA, United States

## ARTICLE INFO

## Article history:

Received 15 April 2007

Received in revised form

3 August 2007

Accepted 7 August 2007

Published online 20 September 2007

## Keywords:

Nitinol

Fatigue

Constant-life diagrams

Stents

## ABSTRACT

Nitinol self-expanding stents are effective in treating peripheral artery disease, including the superficial femoral, carotid, and renal arteries. However, fracture occurrences of up to 50% have been reported in some stents after one year. These stent fractures are likely due to *in vivo* cyclic displacements. As such, the cyclic fatigue and durability properties of Nitinol-based endovascular stents are discussed in terms of an engineering-based experimental testing program. In this paper, the combined effects of cardiac pulsatile fatigue and stent-vessel oversizing are evaluated for application to both stents and stent subcomponents. In particular, displacement-controlled fatigue tests were performed on stent-like specimens processed from Nitinol microtubing. Fatigue data were collected with combinations of simulated oversizing conditions and pulsatile cycles that were identified by computer modeling of the stent that mimic *in vivo* deformation conditions. These data are analyzed with non-linear finite element computations and are illustrated with strain-life and strain-based constant-life diagrams. The utility of this approach is demonstrated in conjunction with 10 million cycle pulsatile fatigue tests of Cordis SMART Control® Nitinol self-expanding stents to calculate fatigue safety factors and thereby predict *in vivo* fatigue resistance. These results demonstrate the non-linear constant fatigue-life response of Nitinol stents, whereby, contrary to conventional engineering materials, the fatigue life of Nitinol is observed to increase with increasing mean strain.

© 2007 Elsevier Ltd. All rights reserved.

## 1. Introduction

Implantation of superelastic Nitinol stents after balloon angioplasty has demonstrated superior clinical outcomes for treatment of peripheral arterial disease (PAD), compared with conventional balloon angioplasty alone (Schillinger et al., 2006). Clinical outcomes are assessed at various

durations after a stenting or balloon angioplasty procedure by measuring the restenosis rate (the fraction of arteries that have a cross-sectional diameter reduction of more than 50% after the procedure) and patency rate (the fraction of arteries that allow blood flow past the procedure location). Nitinol stents have been shown to improve the effectiveness of PAD treatment of the superficial femoral artery (SFA)

\* Corresponding author. Tel.: +1 510 413 1677; fax: +1 510 413 6806.  
E-mail address: [apfremont@yahoo.com](mailto:apfremont@yahoo.com) (A.R. Pelton).

(Duda et al., 2002; Sabeti et al., 2004; Duda et al., 2005; Sabeti et al., 2005; Duda et al., 2006) with a restenosis rate as low as 17.9% at eighteen months (Duda et al., 2005) and patency rates of more than 85% at 18 months (Henry et al., 1996). In contrast, angioplasty had restenosis rates of 40%–60% after one year (Dormandy and Rutherford, 2000) and stainless steel balloon-expandable stents had patency rates of 54% after one year (Gordon et al., 2001). Although Nitinol stents appear to be beneficial for treatment of PAD, there is a growing concern about observations of fractures during follow-up procedures (Allie et al., 2004). A series of articles in *Endovascular Today* focused on PAD and the unique environment of the SFA that may explain the unexpectedly high incidence of stent fracture. Jaff (2004) pointed out that the SFA is at risk for PAD because it is an especially long vessel and is surrounded by two major flexion points. He illustrated the possible non-pulsatile forces exerted on the SFA that include torsion, compression, extension and flexion. Smouse et al. (2005) also discussed the biomechanical forces in the femoropopliteal arteries and focused on the reports of stent fractures.

In the past few years a number of reports based on clinical studies have begun to elucidate the impact of SFA fractures on restenosis rates. For example, several reports have been made of fractures in the SFA as part of the SIROCCO trial (Duda et al., 2002, 2005, 2006). Specifically, Duda et al. (2005, 2006) observed fracture rates of 17% at 6 months and 26% at 18 months with in stent restenosis rates of 4.7% at 6 months and 21.9% at 24 months. Furthermore, Scheinert et al. (2005) demonstrated that not all Nitinol stent designs have the same *in vivo* fracture rate; fractures occur in up to 50% of procedures with some stents and may induce clinically relevant restenosis.

The FDA has long been concerned with the durability of stents. The 1995 FDA Guidance Document for Intravascular Stents recommended benchtop pulsatile fatigue testing of stents deployed into mock arteries under physiological systolic/diastolic pressure cycles at accelerated frequency relative to cardiac rhythm (FDA, 1995). According to this 1995 guideline, the fatigue durability requirement would be achieved if fatigue fractures did not occur in 400 million cycles, or an equivalent of 10 years at physiologically relevant conditions of pulsatile pressure and mock artery compliance. This approach is termed “test-to-success” because stents are deemed to have passed if they withstand 400 million cycles without a single fracture. However, this method is under serious debate within ASTM (2006a) and ISO (2005) standards committees because it is contrary to more contemporary engineering approaches often employed to predict fatigue lifetimes. Other safety-critical industries, such as aerospace and automotive, have long used a “test-to-fracture” approach; they fracture devices under a range of conditions, including those exceeding expected service conditions, so that a “fatigue–failure” map can be developed. These maps are then used to predict fatigue life of the engineering components under combinations of cyclic conditions (i.e., duty cycles) and material conditions (Mitchell, 1996). Accordingly, the 2005 FDA Guidance Document for Intravascular Stents recommends that extensive fatigue-life analyses be conducted on the stent material in order to determine relevant parameters, such as an “endurance

limit” as well as constructing a constant-life diagram<sup>1</sup> for stents (FDA, 2005). Consequently, this Guidance Document sets a necessary direction for the medical device industry to characterize stents with a “test-to-fracture” methodology under a variety of deformation conditions. As such, the key to understanding Nitinol-based stent fatigue and durability is to establish the Nitinol *fatigue properties* that are mainly material- and surface condition-dependent and the *stent durability properties* that are design- and material-dependent.

A more rigorous understanding of Nitinol fatigue behavior and *in vivo* deformations will lead to stents that are more fatigue resistant. Therefore, the purpose of this paper is to establish the fatigue properties of Nitinol stent subcomponents as well as a methodology for the durability assessment of the Cordis SMART Control<sup>®</sup> stent subjected to pulsatile fatigue. A subsequent paper will address the non-pulsatile musculoskeletal deformation conditions, also within the context of “test-to-fracture” methodology described herein. In this paper, we will focus on two important contributing factors to pulsatile fatigue:

1. Stent oversizing, i.e., the difference between the labeled stent diameter and the vessel inner diameter.
2. Pulsatile motion of the stented vessel due to the cardiac cycle.

## 2. Materials and methods

Self-expanding peripheral stents were manufactured from Nitinol thin-walled tubes with a composition of 50.8 at% Nickel–49.2 at% Titanium (Ni<sub>50.8</sub>Ti<sub>49.2</sub>) in accordance with the specifications of ASTM 2065-05 (ASTM, 2005). The tubes were laser-machined and subsequently expanded and thermally shape-set into their final dimensions, as illustrated by the SMART stent shown in Fig. 1(a). A 9 mm diameter stent with this design has approximate dimensions of: strut width,  $w = 120 \mu\text{m}$ , wall thickness,  $t = 200 \mu\text{m}$ , and strut length,  $L = 2 \text{ mm}$ , as illustrated in Fig. 1(b). These design and manufacturing conditions are similar to those of other Nitinol self-expanding peripheral stents (Bonsignore, 2004) with an Austenite finish ( $A_f$ ) temperature of  $\sim 30^\circ\text{C}$ , measured by bend and free recovery methods (ASTM, 2006b). The interested reader is referred to the literature for the importance of the transformation temperatures, in particular the  $A_f$ , on the mechanical behavior of Nitinol (Pelton et al., 2000).

### 2.1. Finite element analysis

Non-linear Finite Element Analysis (FEA) was used to determine peak local strains in the stent subjected to physiological artery compliance, oversizing, and pulse pressures. In addition, results from FEA were used to predict

<sup>1</sup> The constant-life diagram is sometimes given the misnomer of “Goodman diagram” because of the well-known Goodman relationship between mean stress and stress amplitude. However, the term “constant-life diagram” is more applicable for Nitinol with mean strain and strain amplitude.

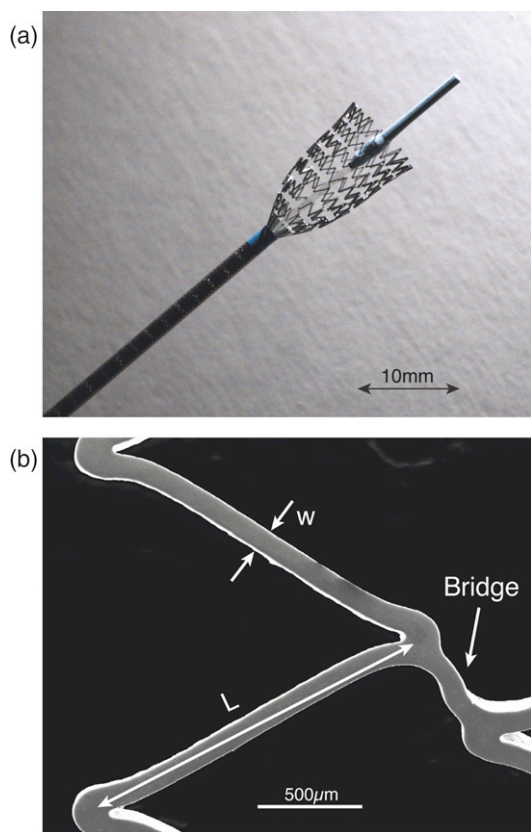


**Fig. 1 – (a) Cordis SMART<sup>®</sup> stent shown partially deployed from the delivery system. Note the repeating pattern of “strut Vs” connect by bridges. (b) Scanning electron microscopy image of a SMART “strut V” illustrating the strut length,  $L$ , width,  $w$ , and bridge. The stent wall thickness,  $t$ , is projected into the page.**

peak local strains for a range of oversizing and pressures that map the cyclic-strain domain beyond physiologically relevant conditions. With FEA, the same maximum local strains that govern fatigue behavior can be used to define test conditions for a stent and stent subcomponent; the use of the strain normalization as a basis of comparison is especially important because of the non-linear nature of mechanical behavior, whereby the total strain is a combination of elastic, martensitic phase transformation, and plasticity.

Mechanics relations have been derived for the idealized stent geometry (small ratio of strut width to length) and for asymptotic solutions for Nitinol (Rebello et al., 2000; Gong et al., 2004). However, due to the complex nature of the stent crimp-deploy process as well as *in vivo* pulsatile cycling, it is necessary to conduct a relatively sophisticated finite-element analysis to track the nominal forces, nominal displacements, and local strains within the stent. The commercial FEA package ABAQUS<sup>®</sup>/Standard version 6.2-1 was used in combination with the user-defined material subroutine (UMAT)/Nitinol-3D version 4.1-2 for these computational analyses. Symmetrical boundary conditions were enforced at the symmetry surfaces and a single node was fixed to prevent out-of-plane rigid body translation. The non-linear mechanical and thermal input properties for

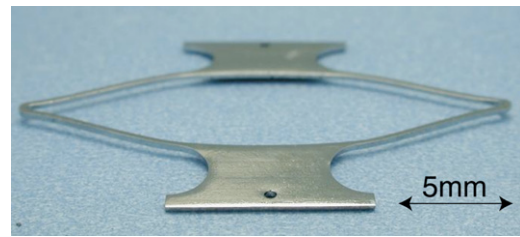


**Fig. 2 – A Nitinol diamond-shaped specimen manufactured from a laser-machined microtube. Specimens are thermally processed and electropolished similar to endovascular stents. Note the geometric similarities of the “strut Vs” in the diamond sample to the SMART stent shown in Fig. 1.**

the Nitinol UMAT were derived from uniaxial tension and compression tests from Nitinol wire and tubing with an  $A_f$  of 30 °C tested at 37 °C (Gong et al., 2004). These computational methods were used to analyze stents subjected to benchtop pulsatile testing as well as for stent subcomponent fatigue testing in the following sections.

## 2.2. Stent subcomponent fatigue specimens

The *in vivo* pulsatile fatigue motion of a Nitinol self-expanding stent can be simulated by observing the behavior of a “strut V” stent subcomponent subjected to cyclic loading. Fig. 2 shows a diamond-shaped stent subcomponent that was specially designed to assess pulsatile fatigue properties of the Nitinol stents. This diamond specimen is based on the SMART stent geometry and therefore has scaled stent dimensions of strut length (8 mm), strut width (330 µm) and strut thickness (350 µm). The tabs at the top and bottom of the diamonds were designed to provide proper alignment, structural stability, reduction of axial buckling, and secure gripping during laboratory testing. The test specimens were laser-machined from Ni<sub>50.8</sub>Ti<sub>49.2</sub> tubing (4.67 mm outside diameter with 0.38 mm wall thickness) and were processed at 500 °C for approximately 10 min and water quenched to achieve a target  $A_f$  of 30 °C similar to the SMART stent. Thereby, the diamond specimens represent, as closely as possible, the material properties and relative geometry of the actual product. A total of 432 specimens were tested with various combinations of mean and strain amplitudes.

A closed-loop, electro-mechanical desktop test system (EnduraTEC ELF<sup>TM</sup>/3200) with an integrated break detection system was used to perform the diamond fatigue tests. Up to four specimens were tested simultaneously at a frequency of 50 Hz under maximum and minimum displacement control. Fig. 3 shows the specimens mounted in a custom-built fixture. Since alignment is critical for uniform strain distribution, the mounted specimens were visually setup and then checked with an external laser micrometer to detect out-of-plane movement. No evidence of specimen buckling was observed during testing. An environmental chamber with a temperature controller, an air-heating fan, and Type T thermocouple, was used to maintain a

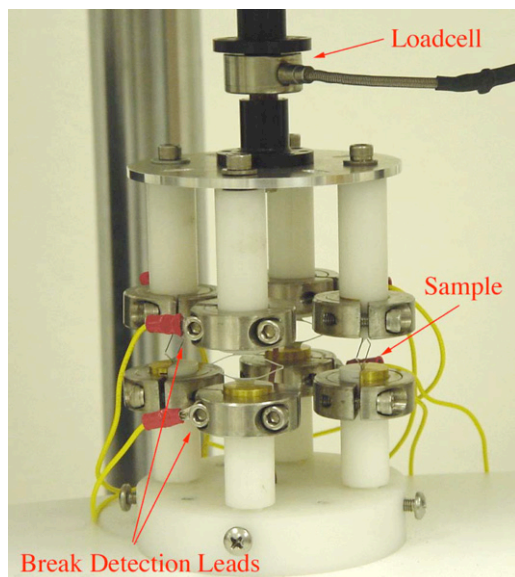


**Fig. 3 – Customized fixture used to fatigue test the Nitinol diamond specimens. Up to four specimens were tested simultaneously under identical conditions of mean strain and strain amplitude. Fracture is monitored for each specimen with an external detection system.**

37 °C test temperature.<sup>2</sup> Before cyclic testing, a single force–displacement cycle was recorded to ensure that the parameters were correctly selected and that the specimens were properly fixtured. All fatigue tests were performed either to fracture or to 10 million cycles (i.e., “run out”).

### 2.3. Pulsatile fatigue of SMART stents

A closed-loop, electro-mechanical stent/graft test system (EnduraTEC Stent/Graft Test System, Model #9010-8), was used for the stent pulsatile fatigue tests. The 10 mm diameter × 40 mm length SMART stents were laser-machined and subsequently processed from 1.8 mm outside diameter and 0.24 mm wall thickness Ni<sub>50.8</sub>Ti<sub>49.2</sub> tubing with a resultant  $A_f = 26\text{--}32$  °C. The stents were radially crimped to 3 mm in an isopropyl alcohol bath cooled to –40 °C and deployed into Dynatek Delta latex mock arteries with inner diameter dimensions between 7 and 9 mm and compliance values of 5%–10% (per 100 mm Hg pressure). Large oversizing and compliance is needed to reach strains that cause fracture during testing, but these values exceed physiologically relevant conditions. The stented mock arteries were filled with phosphate buffered saline solution with pH 7.4 and at 37 °C. A laser micrometer was used to determine the maximum and minimum diameters of the stented mock arteries at the selected maximum and minimum pulse

pressures. The tests were conducted at 30 Hz per ASTM recommendations (ASTM, 2006a) until the stents fractured or 10 million cycles was achieved.

## 3. Results and discussion

### 3.1. In vivo stent deformation

The deformation of a stent follows the radial force–diameter response of a 10 mm SMART (manufactured diameter is approximately 10.5 mm) is depicted in Fig. 4 during radial crimping into the catheter and subsequent deployment of the stent into the artery. The stent is constrained by the arterial wall, such that its diameter is less than the labeled or fully expanded stent diameter; therefore, the stent exerts a chronic outward force (COF) on the arterial wall (Duerig et al., 2000). The effect of this oversizing is illustrated in Fig. 5, where a 9 mm SMART stent that was deployed into 9 mm, 6 mm, and 3 mm inner diameter (ID) silicone mock arteries that are rated with 6% compliance per 100 mm Hg in accord with ASTM (2006a). The 9 mm diameter in Fig. 5(a) represents the diameter and geometric relationships of the unconstrained stent, resulting in an enclosed angle between the struts of approximately 63°. In comparison, when the stent is deployed into a 6 mm vessel (Fig. 5(b)), the force balance between the stent and mock artery results in a lumen diameter of about 6.8 mm and enclosed angle of 32°. The 3 mm constrained diameter in Fig. 5(c) represents an unrealistic extreme case of oversizing; the stented tube diameter is 4.2 mm with an enclosed angle of 13°. The geometric relationships between the angular change and resultant strain are discussed in the Appendix. When implanted, superelastic Nitinol stents tend to “breathe” with the arterial pulse pressures from the cardiac cycle with resultant diastolic and systolic balanced diameters. For the conditions illustrated in Fig. 4, the stent cycles between 9.6 mm (systolic, or maximum diameter at peak blood pressure) and 9.3 mm (diastolic, or minimum diameter), which represent clinically relevant diametral changes in the SFA as discussed subsequently in Section 3.4. This cyclic diameter change can thus be envisioned as partial opening and closing of the “strut V” about a mean position. At high pressure (systole) and minimal oversizing, the “strut V” is open (large angle), while at low pressure (diastole) and large oversizing, the “strut V” narrows. Therefore, both a mean strain from oversizing and cyclic strains from the cardiac rhythm are induced in the stent.

After implantation, the fatigue performance due to the cardiac cycle is determined by the stent diameter at systolic and diastolic pressures. Based on mechanics, there are direct linear relations between the stent diameter,  $D$ , the strut displacement,  $\delta$ , and the maximum principal strain,  $\varepsilon$ :

$$D \propto C_1 \delta \propto C_2 \varepsilon,$$

where;  $C_1$  and  $C_2$  depend on the stent geometry and will be discussed in the Appendix. The resultant stent diameter is controlled by the patient's anatomy, the cardiac cycle, and the physician selection of the initial stent diameter and design. As such, the maximum principal strain that results from these factors of patient anatomy

<sup>2</sup>High-frequency testing in air may induce non-adiabatic heating conditions on the specimens. However, it has been shown that testing of superelastic Nitinol stent material at elevated frequencies in air produces the same fatigue response as *in vivo* conditions (i.e. ~1 Hz and slightly basic pH aqueous environment). (Stankiewicz et al., 2007; Robertson and Ritchie, 2007b).

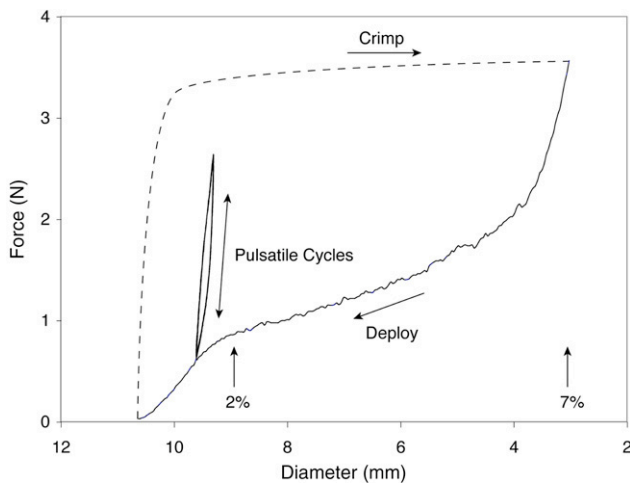


**Fig. 4 – Force–displacement diagram of a radial crimp–deploy process with cyclic displacement due to pulse pressures. The dotted curve is representative of the crimp portion of the curve, whereas, the deploy- and cyclic-portion of the curve are data from a 10 mm SMART during a simulated deployment to 9.6 mm and cycles to 9.3 mm. The initial linear-elastic crimping process may be modeled with traditional mechanics of a “strut V”, whereas the loading and unloading plateau regions must use more complex analyses with finite-element analysis. Approximate strain values of 2% and 7% are shown on the diagram for comparison.**

and physician selection directly influences the stent fatigue performance. Moreover, the derived relations between stent diameter, strut displacement, and strain allow the use of subcomponent geometry fatigue testing to predict pulsatile fatigue performance of the stent, as discussed in the next section.

Before we discuss the results from the fatigue tests, it is instructive to address the primary question that arises, “What is the best *in vitro* method to simulate the *in vivo* pulsatile fatigue environment that the Nitinol stents experience”? In general, both stress-based and strain-based approaches provide insight into the mechanisms of fatigue behavior to predict lifetimes and the appropriate choice often depends on the specifics of the specimens and test environment. Shang et al. (1998) suggested that the fatigue process may be divided into five stages: early microstructural damage, microcrack nucleation, short-crack propagation, macrocrack propagation, and final crack fracture. Stress-based fatigue analyses are clearly preferred in the presence of microscopic surface flaws (e.g. inclusions, grain boundaries, and surface imperfections) or existing cracks that create stress concentrations that can promote fatigue-crack nucleation. When the size of these flaws is equal to, or greater than, the so-called critical flaw length ( $a_{crit}$ ), it necessitates the use of stress-based mechanics solutions to quantify the fatigue and fracture behavior (Robertson and Ritchie, 2007a). In fact, due to the anisotropic mechanical response of stent materials, such as Nitinol or 316 Stainless Steel, even grains themselves can act as flaws and therefore offer nucleation sites for cracks. For example,

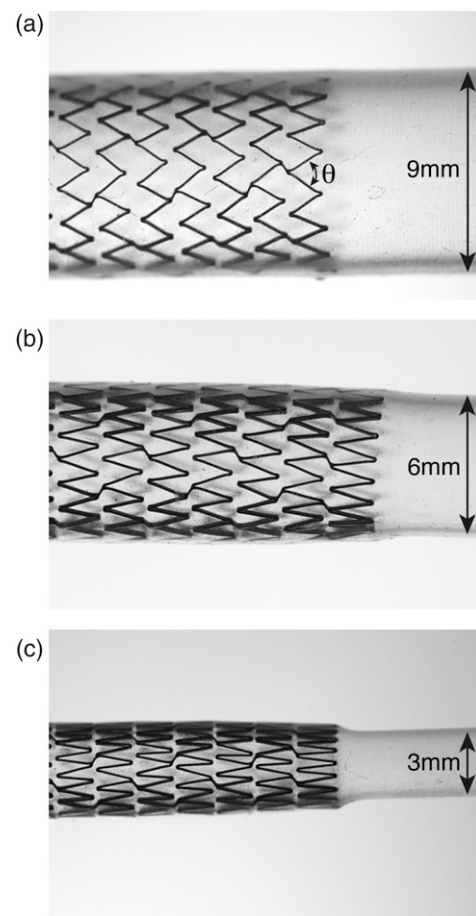


**Fig. 5 – Illustrates the effect of deploying a 9 mm SMART stent into 9 mm (a), 6 mm (b), and 3 mm (c) silicone mock vessels, respectively. The amount of oversizing results in a change in the mean position and enclosed angle,  $\theta$  of the “strut V” structures in the stent.**

the relatively large grains in balloon-expandable 316 Stainless Steel stents provide stress-concentrations representing a large portion (~10%) of the overall stent wall thickness, and therefore must be adequately addressed. In these cases stress-based solutions are shown to successfully predict crack initiation (Wiersma and Taylor, 2005). Conversely, when flaws are smaller than  $a_{crit}$  the contribution of the stress concentrations are minimal and the nucleation of cracks is instead dominated by the cumulative damage of the intrinsic material. Under these conditions, it is acceptable to use either stress- or strain-based mechanics criterion, whichever is more appropriate to simulate the end-use application. When quantifying the fatigue behavior of the stent-like Nitinol specimens herein, the strain-based mechanics criterion was determined to be more appropriate for four reasons:

1. The unique non-linear shape of the monotonic stress-strain curve of superelastic Nitinol lends itself to strain-control tests. For example, with reference to Fig. 4, radial deformation of a stent exhibits two distinct elastic regions. During initial crimping, the stent has a linear-elastic region up to a critical stress. Above this stress, the deformation is accommodated by a reversible

martensitic phase transformation. Under ideal conditions, this transformation occurs at a single value of applied stress, i.e., the stress plateau is perfectly flat (Robertson et al., 2007). When the crimped stent is subsequently deployed, there is an elastic recovery response with a modulus that is affected by the contributions of both austenite ( $E_A$ ) and martensite ( $E_M$ ), where  $E_A \sim 2E_M$  (Pelton et al., 2000). The martensite re-transforms to austenite on the (nominally flat) unloading plateau. Therefore, due to the non-unique stress values, it is more appropriate to conduct testing in deformation (strain) control when the deformation reaches the plateau stress.

2. *In vivo* pulsatile conditions in peripheral self-expanding Nitinol stents are considered to be under displacement-control; see, for example, the methods outlined in ASTM (2006a). Furthermore, non-pulsatile conditions in peripheral arteries are characterized by changes in length or angle that are aligned with strain-controlled fatigue analysis (Cheng et al., 2006).
3. The thermomechanical processing of Nitinol tubing and devices results in a grain size of approximately 100 nm in the stents and stent subcomponents evaluated in this study. As such, the average number of grains per cross-section is  $\sim 1000$  (compared with typical Stainless Steel stent material that has  $\sim 10$  grain diameters per section). The small grain size of Nitinol is two orders of magnitude smaller than the calculated critical flaw size (15–50  $\mu\text{m}$ ) for this material (Robertson and Ritchie, 2007b); therefore stress-concentration effects from grains are negligible. Furthermore, once a crack is nucleated in Nitinol there is a very minimal period of short crack growth before the critical size is reached. Catastrophic failure then rapidly ensues because of the small cross-sections in these medical devices. Consequently, there is minimal time for conventional long crack formation and subsequent growth where contemporary fracture mechanics would be applicable. Shang et al. (1998) were successful in applying a strain-based fatigue analysis to the short-crack initiation regime.

### 3.2. Stent subcomponent fatigue analysis

Subcomponents with a single “strut V” (see Fig. 2) were compressed to various displacement magnitudes to simulate the radial compression of a stent. The force–displacement experimental results agree reasonably well with FEA predictions (Rebello and Perry, 2000; Gong et al., 2004). The FEA-generated displacement–nominal strain relationships were used to obtain the mean strains and strain amplitudes for each test condition. Fig. 6(a) illustrates the color-coded strain distribution map for a diamond specimen that was vertically compressed by 4 mm, corresponding to a maximum principal strain of 4.8% strain. It should be noted that the strain distribution and the location of the maximum principal strain is generally consistent between this idealized subcomponent and an actual oversized stent as shown in Fig. 6(b). Furthermore, the non-linear FEA is used as a foundation of the strain-based fatigue analysis since the first cycle is considered to provide the worst-case stress-strain conditions. For example, Tolomeo et al. (2000)

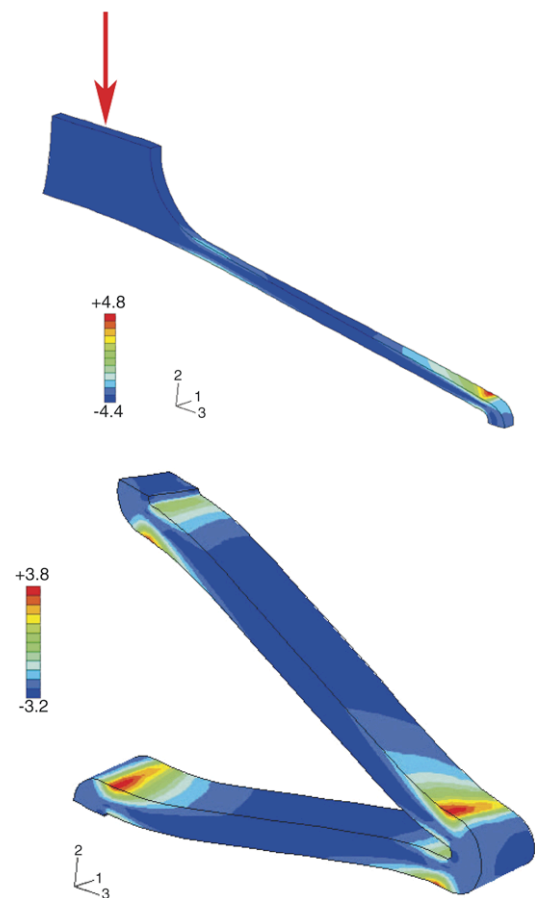


**Fig. 6 – (a) Finite-element analysis strain distribution map of quarter symmetry of a diamond specimen displaced to  $-4$  mm (compression) that corresponds to a maximum principal strain of a global strain of 4.8%. The arrow represents the direction of testing compression comparable to that experienced by stents under a mean strain due to vessel oversizing. (b) Finite-element analysis of the maximum principal strain of a SMART stent radially displaced. Note that the highest strain location is identical to that observed in the diamond specimen in Fig. 6(a).**

demonstrated that cyclic stability of thermomechanically processed Nitinol is achieved in relatively few cycles.

The microscopic-size scale of these stents and stent subcomponents could introduce stress/strain gradients much different from a bulk-material test specimen. Due to these dimensions, both the stents and stent subcomponents should be considered to be predominately non-plane-strain conditions (Robertson et al., 2007). Indeed, from the plane-stress or plane-strain perspective, it is well-established that smaller dimensions lead to artificially-elevated fracture toughness values due to the modified state of stress triaxiality immediately ahead of the propagating crack.

Fig. 7(a) shows the strain amplitude vs. cycle-to-fracture results (strain-life) for conditions of zero-mean strain (cycling about the neutral position); this condition of zero-mean strain is not clinically relevant but provides a basis for comparison with greater mean strains. Only conditions that led to fracture are shown in this figure; fatigue conditions that survived

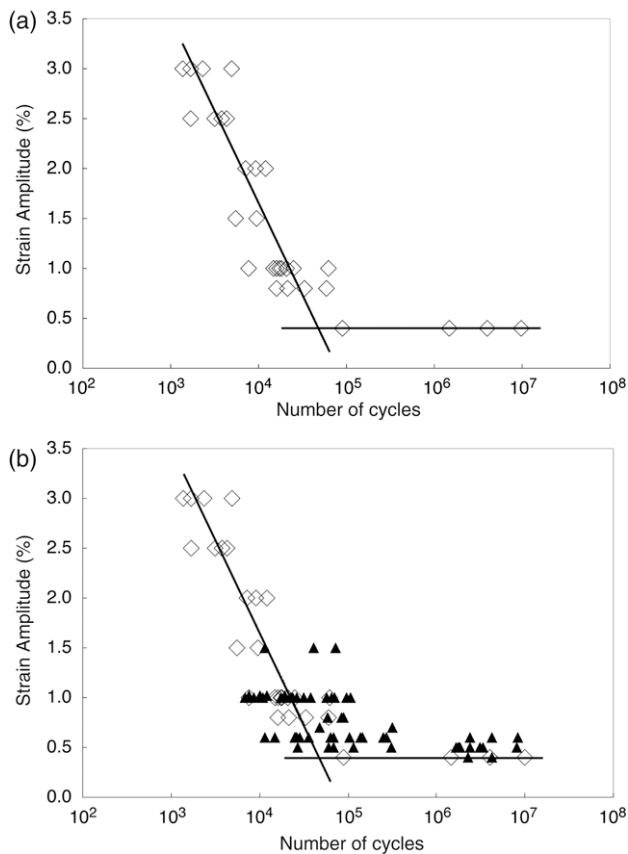


**Fig. 7 – (a) Strain amplitude vs. fatigue data (strain-life) for conditions that led to fracture for zero-mean strain are presented. The diagram can be separated into low-cycle ( $10^3$ – $10^5$  cycles) and high-cycle ( $\geq 10^5$  cycles) regions. The low-cycle data fit well with a power-law slope of  $-0.49$ , as represented by the line. The fatigue strain limit at the high-cycle data is  $0.4\%$ , corresponding to the lowest strain amplitude where fractures were observed. (b) shows non-zero mean strain data superimposed on the zero-mean data.**

$10^7$  cycles are shown in Fig. 8. For this zero-mean condition, fatigue fracture did not occur below cyclic conditions of  $\pm 0.4\%$  strain in  $10^7$  cycles. These data appear typical of engineering alloys that have a low-cycle (typically  $\leq 10^5$  cycles) region at high strain amplitude; these low-cycle data can be fit to a power-law slope of  $-0.49$ , comparable to that observed by Tolomeo et al. (2000). The low-strain amplitude at high cycles ( $\geq 10^5$  cycles) approaches an asymptotic “fatigue limit (run out)” of  $\pm 0.4\%$ . We will use this value of  $\pm 0.4\%$  strain amplitude to calculate a stent fatigue safety factor in Section 3.4.

### 3.3. Effects of mean strain

In order to simulate the effects of *in vivo* stent oversizing, the diamond-shaped subcomponent specimens were tested at various levels of compressive mean strain and strain amplitude to determine the effects on fatigue life. The non-zero-mean strain diamond fatigue data are superimposed on

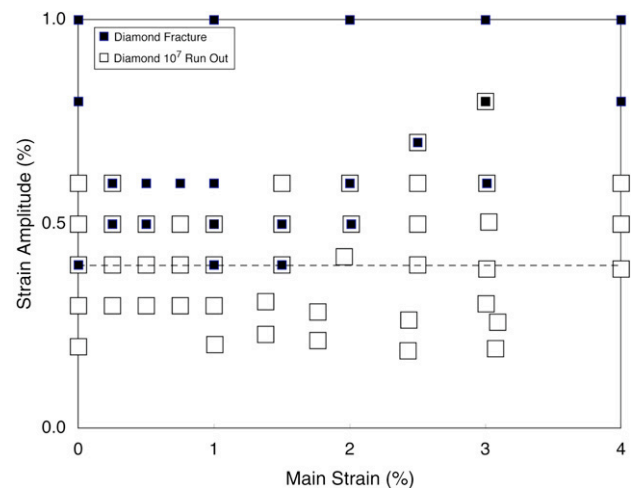


**Fig. 8 – Constant-life diagram from the diamond stent subcomponent fatigue testing where the various conditions of mean strain and strain amplitude are plotted. Conditions that survived the  $10^7$  cycle testing are shown as open squares, whereas cyclic conditions that led to fracture  $< 10^7$  cycles are represented with closed squares. The  $10^7$  fatigue strain limit of  $0.4\%$  is illustrated with a dotted line. Note that mean strain does not lead to decreasing fatigue life, unlike conventional linear-elastic materials.**

the zero-mean strain data in Fig. 7(b); those conditions that led to fracture are shown with solid triangles. Fatigue results from test conditions ranging from  $0\%$  to  $4\%$  mean strains and cyclic strain amplitudes from  $\pm 0.2\%$  to  $\pm 1.5\%$  are shown. In general, the trend lines generated from the zero-mean conditions appear consistent with the data for the non-zero-mean conditions.

Per conventional methodologies, we employ the concept of a constant-life diagram to take into account both mean and amplitude contributions for fatigue-safe designs (Mitchell, 1996). For linear-elastic engineering materials, an increasing mean stress (or strain) tends to decrease the fatigue life at constant amplitude. For these materials, the mean vs. alternating test data are generally analyzed with linear models, such as Goodman analysis or more conservatively with the Soderberg analysis. For a given fatigue lifetime both models result in decreasing slopes that define limiting conditions for safe designs. Engineering safety factors can be calculated readily by relating the mean and amplitude conditions under specific conditions to their relative positions on the constant-life diagram, as will be demonstrated below.

The diamond fatigue-life data from Fig. 7 are re-plotted in a more illuminating way as mean strain vs. strain amplitude in Fig. 8. The specimens that survived  $10^7$  cycles under various mean and strain amplitude conditions are shown as open squares, whereas those specimens that fractured are shown as solid squares. The  $10^7$  cycle fatigue limit of  $\pm 0.4\%$  derived from the data presented in Fig. 7 is shown as a dotted line. It is apparent that these data do not exhibit the negative slopes that are traditionally observed for linear-elastic materials. There are several recent investigations

on the mean-strain effects on the fatigue life of stent-like superelastic Nitinol (Tabanlı et al., 1999; Kugler et al., 2000; Tolomeo et al., 2000; Morgan et al., 2004; Pelton et al., 2004), although the specifics of the testing varied. Tabanlı et al. (1999) were the first to observe non-traditional constant-life fatigue behavior on Nitinol microtubing with an  $A_f$  of about  $-5^\circ\text{C}$  with tensile mean strains from 0.25% to 9.31%. They concluded a fatigue strain amplitude of approximately  $\pm 0.2\%$  for all mean strains. Tolomeo et al. (2000) investigated the fatigue properties of “unzipped” stents after laser cutting and processing, but applied “pull” forces rather than “push” forces; i.e., the maximum strains were on the inside of the stent strut rather than the outside as experienced by stents subjected to *in vivo* oversizing and pulsatile conditions. Kugler et al. (2000) studied laser-machined stent-like test specimens from Nitinol microtubing but also applied the fatigue deformation to the incorrect side of the strut to simulate *in vivo* conditions. Morgan et al. (2004) observed that the fatigue life of Nitinol wire increased with increasing mean strain from 2% to 6% for strain amplitudes that ranged from 0.5% to 3.0% in  $38^\circ\text{C}$  Ringers solution. As a final comment, the above investigations based their conclusions on very few data points focused on specific environment conditions.

The present observations indicate clearly that the Nitinol diamond-shaped specimens have a constant fatigue life with a strain amplitude of  $\pm 0.4\%$  up to an applied mean strain of approximately 1.5%. Above a mean strain of 1.5%, the fatigue life appears to increase with increasing mean strain, strongly indicating that the formation of stress-induced martensite is responsible for this desirable behavior. It is not clear at the present time, however, if this is due to microstructural effects of martensite or perhaps to effects of the lower moduli in the stress-induced transformation regime (i.e., decreased hysteresis energy). Recent *in situ* investigations with synchrotron x-ray diffraction provide additional insight in the micro-scale deformation mechanisms of these diamonds (Mehta et al., 2007) as well as for factors that influence crack growth in Nitinol tubes (Robertson et al., 2007).

### 3.4. Physiological conditions and fatigue safety factors

Arteries are known to vary in diameter and compliance properties, such that when they are stented a range of balanced diameters and resultant strains will be imparted to the implanted stent. Likewise, pulse pressure and stent diameter vary and affect the strains in the stent. For the purpose of our illustration, we assume a pulse pressure ( $\Delta P$ ) of 100 mm Hg (systolic minus diastolic pressures), with diastolic ( $D_d$ ) and systolic ( $D_s$ ) diameters of 9.3 mm and 9.6 mm of the stented vessel, respectively (refer to Fig. 4). The maximum principal strain as a function of stented vessel diameter determined from finite-element analysis (Gong et al., 2004) is used to determine the corresponding mean strains and strain amplitudes. At diastole, the applied maximum principal strain of the stent is 1.45%, whereas at systole, the corresponding strain is 0.98%. The mean strain on the stent for these conditions is therefore  $(1.45\% + 0.98\%)/2 = 1.22\%$ , and the strain amplitude is  $(1.45\% - 0.98\%)/2 = 0.24\%$ . If we assume a worst-case scenario (i.e., the fatigue limit)

for the constant-life line at  $\varepsilon$  of 0.4% (Fig. 8), a stent fatigue safety factor (SF) for the conditions discussed above can be calculated as:

$$SF = \frac{\varepsilon}{\varepsilon_a}$$

where;  $\varepsilon_a$  is the cyclic strain amplitude for the stent, 0.24%; the resultant safety factor is therefore 1.7.

Benetos et al. (1993) used ultrasound imaging to determine the femoral artery diameters at diastolic and systolic pressures. They measured an average pulse pressure (systolic minus diastolic pressure) of 62.5 mm Hg with corresponding diastolic ( $D_d$ ) and (unstented) systolic ( $D_s$ ) diameters of 9.14 mm and 9.45 mm, respectively. From these values, they calculated the percent compliance (%C) of the femoral artery as  $\Delta V/\Delta P \sim \Delta D/D$ ; where  $\Delta V$  is the systolic–diastolic change in the volume (approximated as change in diameter,  $\Delta D$ ). As such, the percent compliance change for the femoral artery due to cardiac cycles was calculated as:

$$\%C = \frac{D_s - D_d}{D_d} (\%) = \frac{9.454 - 9.14}{9.14} (\%) = 3.47\%$$

Similar compliance values were found in other studies of the femoral artery properties (Kawasaki et al., 1987). In contrast, the carotid artery was measured to have a compliance of 6.07% at a pulse pressure of 52.7 mm Hg with  $D_d = 6.79$  mm and  $D_s = 7.20$  mm (Benetos et al., 1993). Both the carotid and femoral arteries exhibit substantially less severe  $\Delta P$  and  $\Delta D$  conditions than discussed in the example above; consequently, the peak local strains in the stent of a given geometry are correspondingly less with a greater resultant safety factor.

### 3.5. Stent pulsatile fatigue life

As further validation of the pulsatile fatigue behavior of the SMART stent, a number of pulsatile-to-fracture proof tests were also conducted. Table 1 lists the pulse pressures, tube diameters, and tube compliance. FEA was used to determine the resultant mean strains and strain amplitudes for the 10 mm diameter SMART stents that are also included in Table 1. It should be noted that many of these experimental conditions exceed the physiologic conditions observed *in vivo*; however, these conditions are included in order to map the entire strain space bordering the physiologically relevant conditions. These experimental stent pulsatile fatigue data are overlaid on the diamond fatigue-life data in Fig. 9. The stents fractured at less than 10 million cycles at high mean and high strain amplitude conditions as predicted by the fatigue strain line. The stents survived to 10 million cycles at conditions of approximately 1% mean strain and strain amplitudes between approximately  $\pm 0.2\%$  to  $\pm 0.45\%$  that are closer to physiologic conditions (approximately shown with a shaded grey box) and are consistent with the 0.4% fatigue strain limit line.

**Table 1 – Test conditions of pulse pressure, mock artery size, and % compliance for 10 mm SMART stent pulsatile fatigue data used in Fig. 9**

Diameter (mm)	Tube % compliance	P <sub>max</sub> (mm Hg)	P <sub>min</sub> (mm Hg)	P <sub>ave</sub> (mm Hg)	Mean strain %	Strain amplitude %	Cycles
6	10	200	20	110	2.19	0.79	7,000
6	10	200	10	105	2.47	1.07	10,900
6	10	150	10	80	2.65	0.89	28,577
7	6	150	10	80	2.37	0.98	28,577
7	6	240	20	130	2.36	0.91	41,755
6	10	160	20	90	2.54	0.83	46,009
7	6	240	20	135	2.36	0.91	51,449
6	10	160	10	85	2.62	0.92	54,404
6	10	180	10	95	2.54	1.00	55,612
8	6	250	10	130	1.07	0.56	60,415
6	10	170	30	85	2.46	0.84	67,606
8	6	250	10	130	1.07	0.56	69,785
7	6	290	110	200	1.82	0.65	70,630
7	6	160	10	85	2.65	0.70	75,000
6	10	160	10	85	2.62	0.92	90,000
6	10	190	10	100	2.51	1.03	91,000
6	10	162	95	85	2.08	0.41	104,000
7	6	230	40	135	2.30	0.79	108,693
7	6	240	30	135	2.32	0.86	108,693
6	10	200	10	105	2.47	1.07	109,638
6	10	190	10	100	2.51	1.03	111,176
6	10	190	10	100	2.51	1.03	112,291
6	10	190	40	115	2.14	0.66	115,000
7	6	250	50	150	2.20	0.81	117,000
7	6	200	20	110	2.31	0.75	155,000
6	10	170	10	90	2.58	0.96	208,921
8	8	250	50	150	0.97	0.68	245,000
7	10	160	20	90	1.36	0.52	318,783
7	10	170	20	95	1.36	0.52	318,783
8	6	250	50	150	1.17	0.61	1,382,400
8	6	250	50	150	1.17	0.61	1,382,400
8	8	250	10	130	1.00	0.71	2,816,559
8	8	250	10	130	1.00	0.71	7,287,842
6	10	180	10	95	2.54	1.00	10,000,000
6	10	180	10	95	2.54	1.00	10,000,000
6	10	183	7	95	2.52	1.02	10,000,000
7	6	140	10	75	2.72	0.63	10,000,000
7	6	150	75	112.5	2.64	0.15	10,000,000
7	6	180	10	95	2.57	0.78	10,000,000
7	6	220	50	135	2.29	0.72	10,000,000
7	8	100	40	70	1.99	0.30	10,000,000
7	8	130	20	75	2.00	0.51	10,000,000
7	8	140	10	75	2.02	0.59	10,000,000
7	8	150	50	100	1.77	0.39	10,000,000
7	8	150	50	100	1.77	0.39	10,000,000
7	8	175	50	112.5	1.68	0.48	10,000,000
7	8	175	50	112.5	1.68	0.48	10,000,000
7	10	180	96	138	0.93	0.18	10,000,000
7	10	180	50	115	1.16	0.40	10,000,000
7	10	205	68	136.5	1.01	0.37	10,000,000
7	10	250	10	130	1.24	0.76	10,000,000
7	10	250	10	130	1.24	0.76	10,000,000
8	6	150	50	100	1.15	0.29	10,000,000
8	6	150	50	100	1.15	0.29	10,000,000
8	6	150	50	100	1.15	0.29	10,000,000
8	6	150	50	100	1.15	0.29	10,000,000
8	6	150	50	100	1.15	0.29	10,000,000
8	6	150	50	100	1.15	0.29	10,000,000
8	6	150	50	100	1.15	0.29	10,000,000
8	6	150	50	100	1.15	0.29	10,000,000
8	6	150	50	100	1.15	0.29	10,000,000
8	6	150	50	100	1.15	0.29	10,000,000

(continued on next page)

Table 1 (continued)

Diameter (mm)	Tube % compliance	P <sub>max</sub> (mm Hg)	P <sub>min</sub> (mm Hg)	P <sub>ave</sub> (mm Hg)	Mean strain %	Strain amplitude %	Cycles
8	6	180	40	110	1.10	0.31	10,000,000
8	6	220	20	120	1.10	0.46	10,000,000
7	6	140	10	75	2.72	0.63	10,000,000

### 3.6. Implication of results on life prediction

The results shown in Fig. 9 demonstrate that the diamond testing analysis is a strong indicator of the SMART stent lifetimes for pulsatile fatigue conditions. Moreover, these results demonstrate that strains imposed by pulsatile motion are not sufficiently high to cause fatigue, and is therefore not principally responsible for stent fractures observed in the SFA. To evaluate the cause of fractures, the use of "test-to-fracture" for lifetime predictions must also be conducted for non-pulsatile musculoskeletal deformation conditions. Recent studies have used x-ray computer tomography (x-ray CT) and magnetic resonance angiography (MRA) to measure the *in vivo* displacements of SFA under controlled movements with the intent of developing a better understanding of the displacements and corresponding strains that stents are subjected to in the body (Cheng et al., 2006). While most of the SFA resides in the adductor canal (the tight tunnel formed between the *vastus medialis*, *adductor longus*, *adductor magnus*, and *sartorius* muscles), some parts of the artery are not nearly as constrained. These unconstrained sections may be subject to significant off-axis deflections,

resulting from axial shortening, lack of SFA elasticity, and localized shortening. Preliminary results show, for example, that the total length of a typical SFA undergoes up to  $\sim 215^\circ$  rotation and  $\sim 20\%$  contraction as the leg is fully bent from an initially extended position; correspondingly, every time the knee is flexed, a stent deployed in such an SFA location undergoes severe, multiaxial displacements that are superimposed on the omnipresent pulsatile displacements of the cardiac cycle (Cheng et al., 2006). In terms of a so-called *duty cycle per year*, the relevant displacements and frequencies include pulsatile motion ( $\sim 40$  million cycles per year) plus bending, torsion, and axial motions at a rate of  $\sim 1$  million cycles per year (Silva, 2002). Although there are  $\sim 40$  times more displacement occurrences due to cardiac cycles, the combined non-pulsatile cyclic motions result in far greater displacements, and therefore, have the possibility of inducing significantly greater cumulative fatigue damage. Thus, the next logical and more critical step in determining the durability of Nitinol endovascular stents is to predict the fatigue lifetime when placed in body-specific locations. This analysis requires knowledge of the deformation duty cycle for that location as well as the cyclic material response at the critical locations in the stent design. A subsequent paper will discuss these non-pulsatile factors for Nitinol stent durability.

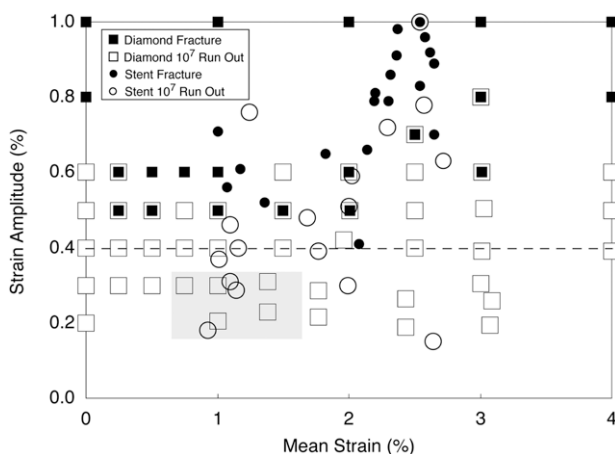


**Fig. 9** – The stent pulsatile fracture data are overlaid on the diamond fatigue data from Fig. 8. The open circles represent test conditions for SMART stents that survived  $10^7$  pulsatile cycles. The closed circles are those conditions that led to fracture of the SMART stent at  $<10^7$  pulsatile fatigue cycles. Note that the stent fatigue testing is consistent with the diamond data, whereby fracture tends to occur above the 0.4% strain amplitude (dotted line) for a range of mean strains. The shaded box represents mean and amplitude strains for typical oversizing and pulsatile fatigue conditions. The test conditions of pulse pressure, mock artery size, and compliance are listed in Table 1.

## 4. Conclusion

Our paper presents results from Nitinol fatigue data collected on diamond-shaped specimens that were cycled to a maximum life of  $10^7$  cycles. Fatigue-life data for these diamond-shaped stent subcomponents were consistent with results for stents. High-cycle data under these conditions indicate a  $10^7$  cycle fatigue strain amplitude limit of  $\pm 0.4\%$ . The effects of mean strain were illustrated on a constant-life diagram and show that there is increased fatigue life at mean strains above about 1.5% compared with the zero-mean conditions. It was speculated that these effects may be due to strain accommodation from stress-induced martensitic transformation. A fatigue-to-fracture approach provides confidence that pulsatile fatigue is not the primary cause of fractures in the SFA. Hence, the same approach must be applied to the musculoskeletal deformation modes that are also active in the SFA to fully assess stent durability.

## Acknowledgements

The authors acknowledge stimulating discussions with C. Bonsignore, Dr. C. Cheng, Dr. T. Duerig and Dr. D. Stöckel, and thank L. Vien for assistance in testing.

## Appendix. Stent design considerations

The SMART stent and many other Nitinol stents are composed of a series of “V-shaped” struts in rows that are connected by “bridges”, as illustrated in Fig. 1(b) (Bonsignore, 2004); as such, these stents may be characterized by the methods described in this article. Duerig et al. (2000) discussed the mechanical and geometric features that influence the performance of self-expanding Nitinol stents. Many of the critical performance attributes, such as *Chronic Outward Force* (COF, defined as the force exerted by the stent against the vessel), and *Radial Resistive Force* (RRF, defined as the external force required to radially compress the stent) may be determined by considering the geometry and motion of a single strut pair; i.e., a “strut V”. The relative COF is proportional to the structural stiffness and therefore can be approximated by (Duerig et al., 2000):

$$\text{COF} \propto \text{Stiffness} \approx \frac{tw^3}{L^3}, \quad (\text{A.1})$$

where:  $t$ ,  $w$ , and  $L$  are respectively the strut thickness, width and length as shown in Fig. 1(b). This relationship relates the stent geometry to stent material properties and illustrates the strong and inverse influence to the cube of strut length and directly to the cube of strut width. As such, for a given design, minor adjustments to  $w$  and  $L$  can be made to fine tune the stiffness and thereby the COF. Of course, the possible range of values is constrained by other desirable stent properties that are affected by  $w$  and  $L$ , such as the crimped diameter of the stent.

From simple mechanics (Roark and Young, 1975), the corresponding deflection perpendicular to the strut,  $\delta$ , and strain,  $\varepsilon$ , for these “strut V” motions can be approximated by:

$$\delta_{\text{tot}} = 2L \sin \frac{\Delta\theta}{2}, \quad (\text{A.2})$$

where:  $\Delta\theta$  is the enclosed angle change (see Fig. 5), and  $\delta_{\text{tot}}$  is the strut tip displacement. The total tip displacement is therefore proportional to the strut length and the enclosed half angle. From geometric considerations and when the angle change between the struts is small,  $\delta_{\text{tot}}$  is approximately related to the stent diameter change as:

$$\delta_{\text{tot}} = \frac{\pi(\Delta D)}{M}, \quad (\text{A.3})$$

where:  $\Delta D$  is the difference between the unconstrained and *in vivo* constrained diameters, and  $M$  is the circumferential number of strut cells per strut row in the stent design. For most tube-based Nitinol stents,  $\Delta D$  is approximately equal to the oversizing of the stent *in vivo*. The strain is related to the change in relative strut tip displacement in the following form:

$$\varepsilon = Z \left( \frac{\delta_{\text{tot}} w}{L^2} \right). \quad (\text{A.4})$$

$Z$  is a dimensionless constant in superelastic Nitinol when  $\varepsilon$  is confined to  $\varepsilon \leq \varepsilon_0 \approx 1.5\%$  (i.e. in the linear elastic, not the superelastic regime) in Fig. 2 and when both strut angle and the ratio of  $w/L$  are small. At strains greater than  $\varepsilon_0$ ,  $Z$  is a function of the material non-linearity; this will be discussed in more detail below.

Combining Eqs. (A.3) and (A.4), we relate the *in-vivo* strain to the stent design and to the oversizing in the form:

$$\varepsilon = Z \frac{\pi(\Delta D) w}{M L^2}. \quad (\text{A.5})$$

This equation demonstrates that a number of geometric factors impact the stent strain. From a design standpoint, an increase in  $M$  or decrease in  $w$  will result in a moderate strain reduction and thus may lead to increased fatigue life. Clearly, however, strut length has the greatest influence on strain for given conditions of oversizing, number of struts, and strut width. For a specific stent design, strain (and therefore fatigue resistance) is greatly reduced by even a slight increase in strut length. It is important to note however, that for a given design a change in strut length to decrease strain (Eq. (A.4)) will also decrease COF (Eq. (A.1)).

## REFERENCES

- Allie, D., Hebert, C., et al., 2004. Nitinol stent fractures in the SFA. *Endovasc. Today* (July–August), 22–34.
- ASTM, 2005. F 2063–05, Standard specification for wrought nickel-titanium shape memory alloys for medical devices and surgical implants. ASTM International.
- ASTM, 2006a. F2477-06, Standard test method for *in vitro* pulsatile durability testing of vascular stents. ASTM International.
- ASTM, 2006b. F2082–06, Standard test method for determination of transformation temperature of nickel-titanium shape memory alloys by bend and free recovery. ASTM International.
- Benetos, A., Laurent, S., et al., 1993. Arterial alterations with aging and high blood pressure. *Arterioscler. Thromb.* 13, 90–97.
- Bonsignore, C., 2004. A decade of evolution in stent design. In: Pelton, A.R., Duerig, T.W. (Eds.), *SMST 2003: International Conference on Shape Memory and Superelastic Technologies*. International Organization on SMST, Pacific Grove, CA, pp. 519–528.
- Cheng, C.P., Wilson, N.M., et al., 2006. *In vivo* MR angiographic quantification of axial and twisting deformations of the superficial femoral artery resulting from maximum hip and knee flexion. *J. Vasc. Interv. Radiol.* 17, 979–987.
- Dormandy, J., Rutherford, B., 2000. Management of peripheral arterial disease (PAD). *J. Vasc. Surg.* 31, s1–s296.
- Duda, S.H., Pusich, B., et al., 2002. Sirolimus-eluting stents for the treatment of obstructive superficial femoral artery disease: Six-month results. *Circulation* 106, 1505–1509.
- Duda, S.H., Bosiers, M., et al., 2005. Sirolimus-eluting versus bare nitinol stent for obstructive superficial femoral artery disease: The SIROCCO II trial. *J. Vasc. Interv. Radiol.* 16, 331–338.
- Duda, S.H., Bosiers, M., et al., 2006. Drug-eluting and bare nitinol stents for the treatment of atherosclerotic lesions in the superficial femoral artery: Long-term results from the SIROCCO trial. *J. Endovasc. Ther.* 13, 701–710.
- Duerig, T., Tolomeo, D., et al., 2000. An overview of superelastic stent design. *Min. Invas. Ther. & Allied Technol.* 9 (3–4), 235–246.
- FDA, 1995. Guidance document for intravascular stents.
- FDA, 2005. Guidance document for intravascular stents.
- Gong, X.Y., Pelton, A.R., et al., 2004. Finite element analysis and experimental evaluation of superelastic nitinol stent. In: Pelton, A.R., Duerig, T.W. (Eds.), *SMST 2003: International Conference on Shape Memory and Superelastic Technologies*. International Organization on SMST, Pacific Grove, CA, pp. 453–462.

- Gordon, I.L., Conroy, R.M., et al., 2001. Three-year outcome of endovascular treatment of superficial femoral artery occlusion. *Arch. Surg.* 136, 221–228.
- Henry, M., Amor, M., et al., 1996. Clinical experience with a new nitinol self-expanding stent in peripheral artery disease. *J. Endovasc. Surg.* 3, 369–379.
- ISO 25539-2, 2005. Cardiovascular implants—endovascular devices—part 2: Vascular stents.
- Jaff, M.R., 2004. The nature of SFA disease. *Endovasc. Today* (October), 3–5.
- Kawasaki, T., Sasayam, S., et al., 1987. Non-invasive assessment of the age related changes in stiffness of major branches in the human arteries. *Cardiovasc. Res.* 21, 678–687.
- Kugler, C., Matson, D., et al., 2000. Non-zero mean fatigue test protocol for niti. In: Russell, S.M., Pelton, A.R. (Eds.), SMST-2000: Proceedings of the International Conference on Shape Memory and Superelastic Technologies. International Organization on SMST, Pacific Grove, CA, pp. 409–417.
- Mehta, A., Gong, X.-Y., et al., 2007. Understanding the deformation and fracture of nitinol endovascular stents using in situ synchrotron x-ray micro-diffraction. *Adv. Mater.* 19, 1183–1186.
- Mitchell, M.R., 1996. Fundamentals of modern fatigue analysis for design. In: ASM Handbook, Fatigue and Fracture. vol. 19, Materials Park, OH, pp. 227–262.
- Morgan, N.B., Painter, J., et al., 2004. Mean strain effects and microstructural observations during in vitro fatigue testing of niti. In: Pelton, A.R., Duerig, T.W. (Eds.), SMST 2003: International Conference on Shape Memory and Superelastic Technologies. International Organization on SMST, Pacific Grove, CA, pp. 303–310.
- Pelton, A., DiCello, J., et al., 2000. Optimization of processing and properties of medical-grade nitinol wire. In: SMST 2000: International Conference on Shape Memory and Superelastic Technologies. International Organization on SMST, Pacific Grove, CA.
- Pelton, A.R., Gong, X.-Y., et al., 2004. Fatigue testing of diamond-shaped specimens. In: Pelton, A.R., Duerig, T.W. (Eds.), SMST 2003: International Conference on Shape Memory and Superelastic Technologies. International Organization on SMST, Pacific Grove, CA, pp. 293–302.
- Rebelo, N., Hsu, M., et al., 2000. Simulation of superelastic alloys behavior with ABAQUS. In: Russell, S.M., Pelton, A.R. (Eds.), SMST-2000: Proceedings of the International Conference on Shape Memory and Superelastic Technologies. International Organization on SMST, Pacific Grove, CA, pp. 457–469.
- Rebelo, N., Perry, M., 2000. Finite element analysis for the design of nitinol medical devices. *Min. Invas. Ther. & Allied Technol.* 9 (2), 453–462.
- Roark, R.J., Young, W.C., 1975. Formulas for Stress and Strain. McGraw-Hill Book Company, New York.
- Robertson, S.W., Ritchie, R.O., 2007a. In vitro fatigue-crack growth and fracture toughness behavior of thin-walled superelastic nitinol tube for endovascular stents: A basis for defining the effect of crack-like defects. *Biomater.* 28, 700–709.
- Robertson, S.W., Ritchie, R.O., 2007b. A fracture-mechanics-based approach to fracture control in biomedical devices manufactured from superelastic nitinol tube. *J. Biomed. Mater. Res. Part B: Appl. Biomater.* doi:10.1002/jbm.b.30840.
- Robertson, S.W., Mehta, A., et al., 2007. Evolution of crack-tip transformation zones in superelastic nitinol subjected to in situ fatigue: A fracture mechanics and synchrotron x-ray micro-diffraction analysis. *Acta. Mater.* doi:10.1016/j.actamat.2007.07.028.
- Sabeti, S., Schillinger, M., et al., 2004. Patency of femoropopliteal arteries treated with nitinol versus stainless steel self expanding stents: Propensity score-adjusted analysis. *Radiology* 232, 516–521.
- Sabeti, S., Mlekusch, W., et al., 2005. Primary patency of long-segment self-expanding nitinol stents in the femoropopliteal arteries. *J. Endovasc. Ther.* 12, 6–12.
- Scheinert, D., Scheinert, S., et al., 2005. Prevalence and clinical impact of stent fractures after femoropopliteal stenting. *J. Am. Coll. Cardiol.* 45, 312–315.
- Schillinger, M., Sabeti, S., et al., 2006. Balloon angioplasty versus implantation of nitinol stents in the superficial femoral artery. *New England J. Med.* 354 (18), 1879–1888.
- Shang, D.-G., Yao, W.-X., Wang, D.-J., 1998. A new approach to the determination of fatigue crack initiation size. *Int. J. Fatigue* 20, 683–687.
- Silva, M., 2002. Average patient walking activity approaches two million cycles per year. *J. Anthroplasty* 17, 693–697.
- Smouse, H.B., Nikanorov, A., et al., 2005. Biomechanical forces in the femoropopliteal arterial segment. *Endovasc. Today* (June), 60–66.
- Stankiewicz, J.M., Robertson, S.W., et al., 2007. Fatigue-crack growth properties of thin-walled superelastic austenitic nitinol tube for endovascular stents. *J. Biomed. Mater. Res. Part A* 81A, 685–691.
- Tabanlı, R., Simha, N., et al., 1999. Mean stress effects on fatigue of nitinol. *Mater. Sci. Eng. A.* 273–275. 644–648.
- Tolomeo, D., Davidson, S., et al., 2000. Cyclic properties of superelastic nitinol: Design implications. In: Russell, S.M., Pelton, A.R. (Eds.), SMST-2000: Proceedings of the International Conference on Shape Memory and Superelastic Technologies. International Organization on SMST, Pacific Grove, CA, pp. 409–417.
- Wiersma, S., Taylor, D., 2005. Fatigue of materials used in microscopic components. *Fatigue Fracture Eng. Mater. Struct.* 28, 1153–1160.